Communications in Computational Chemistry
Commun. Comput. Chem., Vol. 7, No. 3, 217–225
doi: 10.4208/cicc.2025.152.01
Regular Article

Data-Driven Versus Physics-Informed Neural Networks for Nonadiabatic Semiclassical Mapping Dynamics

Hao Zeng[1,2,3,4] and Xiang Sun[1,2,3,4,5,*]

[1]*Shanghai Frontiers Science Center of Artificial Intelligence and Deep Learning, NYU Shanghai, 567 West Yangsi Road, Shanghai, 200124, China*;

[2]*State Key Laboratory of Precision Spectroscopy, East China Normal University, Shanghai 200062, China*;

[3]*Division of Arts and Sciences, NYU Shanghai, 567 West Yangsi Road, Shanghai 200124,China*;

[4]*NYU-ECNU Center for Computational Chemistry at NYU Shanghai, 3663 Zhongshan Road North, Shanghai 200062, China*;

[5]*Department of Chemistry, New York University, New York, New York 10003, United States.*

[*] Corresponding author: xiang.sun@nyu.edu

Received on 1 June 2025; Accepted on 16 June 2025

Abstract: Semiclassical mapping dynamics offer a computationally tractable approach for simulating nonadiabatic processes in complex molecular systems. This work presents a comparative study of purely data-driven (DD) neural networks and physics-informed neural networks (PINNs) for learning the Markovian propagation of trajectories within the Meyer-Miller-Stock-Thoss (MMST) mapping Hamiltonian framework. Using the spin-boson model as a benchmark, we assess the performance of both approaches in reproducing the nonadiabatic dynamical details for classical mapping model (CMM) and symmetrical quasiclassical (SQC) dynamics. Our results demonstrate that PINNs, which explicitly incorporate the physical equations of motion, significantly outperform DD models, especially when trained with limited datasets. PINNs accurately capture the population dynamics and preserve the physical correlations in phase space, regardless of the underlying neural network architecture (fully connected network or gated recurrent unit) or the specific MMST Hamiltonian formulation. In contrast, DD models exhibit substantial inaccuracies and unphysical behaviors. This clearly shows the key benefit of embedding physical laws into machine learning frameworks to achieve data-efficient, accurate, and reliable simulations of nonadiabatic phenomena.

Key words: machine learning, nonadiabatic dynamics, physics-informed neural network, data-driven approach, mapping Hamiltonian.

1. Introduction

Nonadiabatic dynamics describe the molecular processes involving transitions between multiple electronic potential energy surfaces and are fundamental to a vast array of phenomena in chemistry, physics, and biology. These processes are characterized by the intrinsic coupling of nuclear and electronic motions, which is beyond the scope of the Born-Oppenheimer approximation. They govern the outcomes of photochemical reactions, facilitate charge and energy transfer events, and underpin critical biological functions such as photosynthesis [1–5]. Furthermore, nonadiabatic events are central

to solar energy conversion and the behavior of advanced materials. A deep understanding of these complex mechanisms is therefore indispensable for the rational design of novel molecules and functional materials.

However, despite their commonness, the simulation of nonadiabatic dynamics presents serious theoretical and computational challenges. The primary difficulty stems from the need to treat the coupled evolution of electronic and nuclear degrees of freedom (DOFs) quantum mechanically. It is a task that is computationally prohibitive for most systems, but some low-dimensional models. Consequently, various approximate methods have been developed, though these introduce their own complexities, including numerical stability, error accumulation, and questions about the validity of underlying approximations for certain processes.

In the quest for computationally tractable yet physically sound approaches, semiclassical methods have emerged as an attractive platform, aiming to balance the inclusion of essential quantum mechanical effects with the efficiencies of classical trajectory-based simulations. A cornerstone in this area is the family of semiclassical or quasiclassical methods based on the Meyer-Miller-Stock-Thoss (MMST) mapping Hamiltonian [6,7]. This mapping dynamics formalism provides a prescription to transform a discrete F-level electronic system into an equivalent mapping Hamiltonian. This Hamiltonian is expressed in terms of F continuous Cartesian phase-space variables for the electronic DOFs, and it allows the coupled dynamics of electronic and nuclear motion to be propagated via Hamilton's equations of motion. The MMST Hamiltonian serves as a foundation for diverse semiclassical methods like various linearized semiclassical dynamics (LSC) [8-12], symmetrical quasi-classical (SQC) windowing techniques [13-17], and classical mapping models (CMM) [18-22], to name a few. The specific semiclassical propagation scheme and observable formulation chosen can profoundly influence simulation accuracy, computational cost, and conservation properties, highlighting the complexity beyond the Hamiltonian [23].

Machine learning (ML), particularly techniques based on neural networks (NNs), has rapidly become a powerful tool in computational chemistry, applied to predict molecular properties, accelerate materials discovery, construct accurate potential energy surfaces, and simulate complex system dynamics [24-28]. The application of ML to nonadiabatic dynamics is a rapidly advancing frontier, offering strategies to develop PESs [29,30], directly propagate quantum wavepackets or reduced density matrices (RDMs) [31-33], and learn the evolution of semiclassical or mixed quantum-classical trajectories [32,34,35]. Purely data-driven (DD) NNs, such as convolutional neural networks (CNNs) [36], kernel ridge regression (KRR) [37,38], gated recurrent units (GRUs) [31,39], long short-term memory (LSTM) [33,40,41], and transformer [42] learn input-output relationships directly from large dynamical datasets. While powerful, these models typically require substantial training data and, without explicit encoding of physical laws, may not inherently respect fundamental principles like energy conservation, potentially leading to physically implausible predictions. In contrast, Physics-Informed Neural Networks (PINNs) [43-48] aim to bridge this gap by incorporating known physical laws, often expressed as differential equations or conservation principles, directly into the NN's loss function during training. This can improve data efficiency, enhance generalization, and produce more physically consistent predictions.

The temporal characteristics of dynamics, particularly the distinction between Markovian (future state depends only on the present) and non-Markovian (future depends on history) behavior, also significantly influence ML model design. The propagation of only the electronic RDM is typically non-Markovian if nuclear DOFs are unknown. This aspect was explored in our previous work [31], where we demonstrated from the Nakajima-Zwanzig generalized quantum master equation (GQME)[49,50] that the non-Markovian propagator for the RDM is fundamentally a linear map, provided that the historical information used for training is sufficiently long compared to the system's intrinsic memory time, for which we also proposed an estimator. Subsequent applications to various neural network architectures showed that when this condition of sufficient historical data was met, simpler linear-mapping NNs like linear fully connected networks (FCNs) could achieve high accuracy and even outperform more complex nonlinear architectures such as GRU or hybrid convolutional neural network-LSTM (CNN-LSTM) [32], which might otherwise be prone to overfitting. Instances where nonlinear NNs appeared superior typically corresponded to situations where the provided historical data length was shorter than the system's memory time, thus not conflicting with the underlying linearity of the true non-Markovian propagator. Such non-Markovian ML models, which use a segment of historical dynamics to predict a future time step, are referred to as short-for-long (SFL) type models.

In semiclassical mapping dynamics, however, the total knowledge of electronic mapping variables and nuclear phase space variables is available at each time slice. Training an ML model with this complete instantaneous state information should, in principle, allow for the description of Markovian dynamics, where the next state is predicted solely from the current state, thus simplifying the ML task. Previous work by Lan and coworkers utilized LSTM networks to train SQC mapping dynamics [35] (both electronic and nuclear variables) using short-time windows of trajectory data as input, an approach akin to training for non-Markovian dynamics; their ensemble averages of electronic populations showed good agreement with reference calculations.

In this study, we adopt a distinct Markovian approach to directly compare the effectiveness of purely data-driven NNs (such as FCNs and GRUs) against PINNs for predicting the propagation of nonadiabatic dynamics within the MMST mapping Hamiltonian framework. Importantly, we train our models with only one time step of complete state information (electronic mapping variables and nuclear phase space variables) as input to predict the state at the very next time step, genuinely treating the learning problem as Markovian. In our PINN implementation, which we use as a general term, the known form of the equations of motion (EOM) derived from the mapping Hamiltonian is incorporated into the learning process, while NNs may be employed to learn specific physical terms within these EOMs, such as potential energy surfaces, their gradients, or the zero-point-energy parameter. A primary goal of this study is to use a relatively small training dataset to showcase the potential benefits of incorporating physics-informed properties, i.e., the explicit form of the EOM governing the mapping dynamics, in accurately reproducing the step-to-step propagation. This paper will further detail the theoretical background of the methods, outline the computational approaches and model systems, present a critical discussion of the comparative results, and conclude with key findings and future outlooks.

2. Theory

We start with expressing the general F-state quantum me-chanical Hamiltonian as

$$\hat{H} = \frac{\hat{\mathbf{P}}^2}{2\mu} + \hat{V}(\hat{\mathbf{R}}) = \frac{\hat{\mathbf{P}}^2}{2\mu} + \sum_{j,k}^{F} V_{jk}(\hat{\mathbf{R}})\,|j\rangle\langle k|, \tag{1}$$

where $\{|j\rangle; j = 1, ..., F\}$ are the electronic state basis; $\hat{\mathbf{R}} = (\hat{R}_1, \cdots, \hat{R}_N)$ and $\hat{\mathbf{P}} = (\hat{P}_1, \cdots, \hat{P}_N)$ are the N nuclear coordinates and momenta with mass μ; $\hat{V}(\hat{\mathbf{R}}) = \sum_{j,k}^{F} V_{jk}(\hat{\mathbf{R}})\,|j\rangle\langle k|$ is the electronic Hamiltonian, where $V_{jj}(\hat{\mathbf{R}}) \equiv V_j(\hat{\mathbf{R}})$ is the PES of the j-th electronic state and $V_{jk}(\hat{\mathbf{R}}) = V_{kj}(\hat{\mathbf{R}})$ is the electronic coupling between the j-th and the k-th electronic states ($j \neq k$).

The corresponding primitive Meyer-Miller-Stock-Thoss Hamiltonian is written as [6,7]

$$H(\mathbf{P}, \mathbf{R}, \mathbf{p}, \mathbf{q}) = \frac{\mathbf{P}^2}{2\mu} + \sum_{j,k}^{F} V_{jk}(\mathbf{R}) \left[\frac{1}{2\hbar}(q_i - ip_j) \times (q_k + ip_k) - \gamma\delta_{jk} \right], \tag{2}$$

where $\mathbf{q} = (q_1, ..., q_F)$ and $\mathbf{p} = (p_1, ..., p_F)$ are the position and momentum mapping variables, and γ is the zero-temperature-energy (ZPE) parameter with $\gamma = 1/2$ recovering the full quantum zero-point energy in the original MMST formulation. The population normalization condition reads

$$\sum_{j=1}^{F} \left(\frac{1}{2\hbar} p_j^2 + \frac{1}{2\hbar} q_j^2 - \gamma \right) = 1. \tag{3}$$

With the above relation, Eq. 2 has an equivalent symmetrized form [13]:

$$H(\mathbf{P}, \mathbf{R}, \mathbf{p}, \mathbf{q}) = \frac{\mathbf{P}^2}{2\mu} + \bar{V}(\mathbf{R}) + \frac{1}{2\hbar} \sum_{j,k}^{F} (q_j - ip_j)(q_k + ip_k) \times [V_{jk}(\mathbf{R}) - \delta_{jk}\bar{V}(\mathbf{R})]. \tag{4}$$

Here, the averaged potential energy of all states is denoted as $\bar{V}(\mathbf{R}) = \frac{1}{F}\sum_{j=1}^{F} V_{jj}(\mathbf{R})$. The ZPE parameter does not explicitly show in the symmetrized MMST Hamiltonian, but the ZPE parameter affects the initial sampling for mapping variables. In atomic units, $\hbar = 1$ is adopted, but we leave explicit $\hbar$ here for bookkeeping purposes.

The time evolution for the MMST mapping Hamiltonian is governed by the classical EOM [51], namely Hamilton's equations

$$\dot{\mathbf{q}} = \frac{\partial H}{\partial \mathbf{p}}, \quad \dot{\mathbf{p}} = -\frac{\partial H}{\partial \mathbf{q}}, \quad \dot{\mathbf{R}} = \frac{\partial H}{\partial \mathbf{P}}, \quad \dot{\mathbf{P}} = -\frac{\partial H}{\partial \mathbf{R}} \tag{5}$$

where the dot indicates the time derivative. Inserting the primitive MMST Hamiltonian in Eq. (2) into the above Eq. (5), we obtain the following EOM with explicit γ:

$$\dot{q}_k = \frac{1}{\hbar} \sum_{j=1}^{F} V_{kj}(\mathbf{R}) p_j, \tag{6a}$$

$$\dot{p}_k = -\frac{1}{\hbar} \sum_{j=1}^{F} V_{kj}(\mathbf{R}) q_j, \tag{6b}$$

$$\dot{\mathbf{R}} = \frac{\mathbf{P}}{\mu}, \tag{6c}$$

$$\dot{\mathbf{P}} = -\sum_{j,k}^{F} \frac{\partial V_{jk}(\mathbf{R})}{\partial \mathbf{R}} \left[\frac{1}{2\hbar}(q_j q_k + p_j p_k) - \gamma\delta_{jk} \right]. \tag{6d}$$

In the data-driven approach, the electronic-nuclear variables, denoted as $\mathbf{x} = (\mathbf{q},\mathbf{p},\mathbf{R},\mathbf{P})$, NN directly treats $\mathbf{x}(t)$ as the input and $\mathbf{x}(t + \Delta t)$ as the output for the one-step forward learning without physical information as shown in Fig. 1(a).

In our PINN implementation, we have two versions that correspond to the primitive MMST Hamiltonian (Eq. 2) and the symmetrized MMST Hamiltonian (Eq. 4). The PINN structure is as shown in Fig. 1(b). For example, the EOM of the primitive MMSH Hamiltonian requires the information such as μ, γ, and $\{V_{jk}(\mathbf{R})\}$, which are represented using NNs as follows:

$$\begin{aligned} &\mu \rightarrow \theta_1 \in \mathbb{R}, \\ &\gamma \rightarrow \theta_2 \in \mathbb{R}, \\ &\{V_{jk}(\mathbf{R})\} \rightarrow \theta_3 : \mathbb{R}^N \rightarrow \mathbb{R}^{F^2}, \\ &\left\{\frac{\partial V_{jk}(\mathbf{R})}{\partial \mathbf{R}}\right\} \rightarrow \theta_4 : \mathbb{R}^N \rightarrow \mathbb{R}^{NF^2}. \end{aligned} \tag{7}$$

So we need two individual parameter sets for μ, γ and two different NNs to map N nuclear positions to F^2 and two and NF^2 parameters, respectively. In this case, we rewrite the EOM characterized by NNs as

$$\dot{\mathbf{x}}(t) = \mathcal{M}[\mathbf{x}(t);\, \theta_1,\theta_2,\theta_3,\theta_4], \tag{8}$$

where $\mathcal{M}$ is a propagation map derived by combining Eqs. 6 and 7, with $\{\theta_1,\theta_2,\theta_3,\theta_4\}$ as parameters, $\mathbf{x}$ and $\dot{\mathbf{x}}$ as input and output respectively. To improve accuracy, we propagate $\mathbf{x}$ with fourth-order Runge-Kutta (RK4) algorithm with PINN time derivative $\dot{\mathbf{x}}$.

In the PINN implementation for the symmetrized MMST Hamiltonian, the parameters of EOM are similar to Eq. 7, but need to replace the θ_2 parameter with an NN for the average potential energy

$$\bar{V}(\mathbf{R}) \rightarrow \theta_2' : \mathbb{R}^N \rightarrow \mathbb{R}. \tag{9}$$

In practice, the time step Δt is absorbed into the propagation mapinterms of $\bar{\mathcal{M}} = \Delta t\, \mathcal{M}$ and $\bar{\theta}_i = \Delta_t \theta_i$.

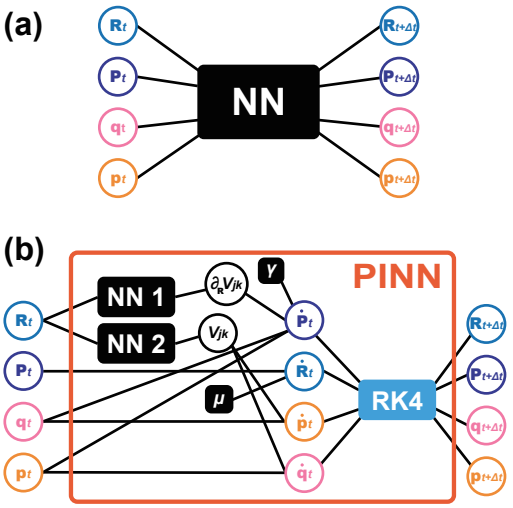

Figure 1. Schematics of (a) data-driven neural network, (b) physics-informed neural network for predicting the nonadiabatic mapping dynamics.

Two types of neural network architectures, FCN and GRU, are tested in both DD and PINN approaches. For a single fully-connected layer, its general expression is

$$\mathbf{y} = f(\mathbf{W}\mathbf{x}+\mathbf{b}), \tag{10}$$

where $\mathbf{x} \in \mathbb{R}^n$ and $\mathbf{y} \in \mathbb{R}^m$ are input and output vectors, respectively, $\mathbf{W} \in \mathbb{R}^{m\times n}$, $\mathbf{b} \in \mathbb{R}^m$ are weight matrix and bias, respectively, f is activation function to generate nonlinearity. An FCN typically consists of multiple fully-connected layers, and a 3-layer FCN is used in this work:

$$\mathbf{h}^{(1)} = \mathrm{sig}[\mathbf{W}^{(1)}\mathbf{x} + \mathbf{b}^{(1)}], \tag{11a}$$
$$\mathbf{h}^{(2)} = \mathrm{sig}[\mathbf{W}^{(2)}\mathbf{h}^{(1)} + \mathbf{b}^{(2)}], \tag{11b}$$
$$\mathbf{y} = \mathbf{W}^{(3)}\mathbf{h}^{(2)} + \mathbf{b}^{(3)}, \tag{11c}$$

where the activation function is chosen as sigmoid $\mathrm{sig}(x) = \frac{e^x}{1+e^x}$, and the hidden layers $\mathbf{h}^{(1)} \in \mathbb{R}^{N_{h1}}$ and $\mathbf{h}^{(2)} \in \mathbb{R}^{N_{h2}}$ have hidden sizes N_{h1},N_{h2}, which determine the sizes of weight matrices and bias together with input and output vectors as in Eq. 10.

GRU is a type of recurrent neural network (RNN) for time series data [39]. In this work, we deal with Markovian dynamics so that historical frames will not be provided, therefore, GRU is reduced to a nonlinear NN. A memory-less GRU layer is expressed as

$$\mathbf{y} = \mathrm{sig}(\mathbf{W}_z\mathbf{x} + \mathbf{b}_z) \odot \tanh(\mathbf{W}_h\mathbf{x} + \mathbf{b}_h). \tag{12}$$

Here, $\mathbf{W}_z$, $\mathbf{W}_h \in \mathbb{R}^{m\times n}$ are the weight matrices, $\mathbf{b}_z$, $\mathbf{b}_h \in \mathbb{R}^m$ are the bias terms, and activation function $\tanh(x) = \frac{e^x - e^{-x}}{e^x + e^{-x}}$. The element-wise product is denoted as $\odot$. In this work, the 3-layer GRU network is constructed by two GRU layers and one linear fully connected layer as below

$$\mathbf{h}^{(1)} = \mathrm{sig}[\mathbf{W}_z^{(1)}\mathbf{x} + \mathbf{b}_z^{(1)}] \odot \tanh[\mathbf{W}_h^{(1)}\mathbf{x} + \mathbf{b}_h^{(1)}], \tag{13a}$$
$$\mathbf{h}^{(2)} = \mathrm{sig}[\mathbf{W}_z^{(2)}\mathbf{h}^{(1)} + \mathbf{b}_z^{(2)}] \odot \tanh[\mathbf{W}_h^{(2)}\mathbf{h}^{(1)} + \mathbf{b}_h^{(2)}], \tag{13b}$$
$$\mathbf{y} = \mathbf{W}^{(3)}\mathbf{h}^{(2)} + \mathbf{b}^{(3)}. \tag{13c}$$

The hidden sizes can be selected arbitrarily like 3-layer FCN.

Now we have described how to propagate the EOM of MMST mapping Hamiltonian using both DD and PINN strategies. We will briefly state how observables are defined in different semiclassical and quasiclassical methods, e.g., CMM [18-22] and SQC [13-17] methods. The main property of interest in nonadiabatic dynamics is the electronic RDM, which is defined as $\hat{\sigma}(t) = \mathrm{Tr}_N[\hat{\rho}(t)]$, where $\hat{\rho}(t)$ is the overall density matrix and $\mathrm{Tr}_N(\cdot)$ is the trace over nuclear DOF. The diagonal elements of RDM represent electronic populations, and the off-diagonal elements represent coherences. Assume the initial state is prepared as $\hat{\rho}(0) = |a\rangle\langle a| \otimes \hat{\rho}_N(0)$ with the initial nuclear density matrix corresponds to equilibrium with respect to $\hat{H}_b$: $\hat{\rho}_N(0) = e^{-\beta\hat{H}_b}/\mathrm{Tr}_N(e^{-\beta\hat{H}_b})$. Denoting the elementary electronic operator $M_{jk} = |j\rangle\langle k|$, the RDM at time t can be written as [11]

$$\sigma_{kj}(t) = \mathrm{Tr}_N\mathrm{Tr}_e[\hat{\rho}_N(0)|a\rangle\langle a|e^{i\hat{H}t/\hbar}\,|j\rangle\langle k|e^{-i\hat{H}t/\hbar}] \equiv C_{MaaMjk}(t). \tag{14}$$

Here, $\mathrm{Tr}_e(\cdot)$ is the trace over electronic DOF. Here, the TCF $C_{MaaMjk}(t)$ is given by [52]

$$C_{MaaMjk}(t) = \int \mathrm{d}\mathbf{R}_0\,\mathrm{d}\mathbf{P}_0\,\mathrm{d}\mathbf{q}_0\,\mathrm{d}\mathbf{p}_0\,\rho_N(\mathbf{R}_0,\mathbf{P}_0)\,\rho_e(\mathbf{q}_0,\mathbf{p}_0) \times M_{aa}(\mathbf{q}_0,\mathbf{p}_0)\,M_{jk}(\mathbf{q}_t,\mathbf{p}_t), \tag{15}$$

where ρ_N and ρ_e denote the nuclear and electronic mapping variable distributions, respectively.

In the CMM method [18-22], the mapping variables $(\mathbf{q},\mathbf{p})$ are sampled on a $(2F-1)$-sphere to satisfy the condition that the total electronic population equals one:

$$S(\gamma): \sum_{j=1}^{F}\frac{1}{2\hbar}(q_j^2+p_j^2) = 1 + F\gamma. \tag{16}$$

The electronic observables at time 0 and t are given by

$$M_{jk}^{(0)}(\mathbf{q},\mathbf{p}) = \frac{1}{2\hbar}(q_j - ip_j)(q_k + ip_k) - \gamma\delta_{jk}, \tag{17}$$

$$M_{jk}^{(t)}(\mathbf{q},\mathbf{p}) = \frac{Q(\bar{\gamma},\gamma)}{2\hbar}(q_j - ip_j)(q_k + ip_k) - \bar{\gamma}\delta_{jk}, \tag{18}$$

where $Q(\bar{\gamma},\gamma) = \frac{1+F\bar{\gamma}}{1+F\gamma}$ and $\bar{\gamma} = \frac{1-\gamma}{1+F\gamma}$. The ZPE parameter of the CMM method is selected as $\gamma = 1/2$ in this work, and in principle, any value in $\gamma > -1/F$ could be allowed, though $\gamma \in (-1/F, 1/2]$ is more recommended [18,20].

In the SQC method [13-17], the Cartesian mapping variables $(\mathbf{q},\mathbf{p})$ are reformulated to action-angle variables $(\mathbf{n},\mathbf{u})$. Using the triangle window functions, the electronic populations and coherences are expressed as

$$M_{jj}^{(\mathrm{SQC})}(\mathbf{n},\mathbf{u}) = w_1(n_j)\prod_{\substack{l=1\\ l\neq j}}^{F} w_0(n_j,n_l),$$
$$M_{jk}^{(\mathrm{SQC})}(\mathbf{n},\mathbf{u}) = e^{i(u_k-u_j)}w_{\frac{1}{2}}(n_j)w_{\frac{1}{2}}(n_k)\prod_{\substack{l=1\\ l\neq j,k}}^{F} w_0(n_j - n_k,n_l). \tag{19}$$

Here, the triangle window functions are defined as $w_a(n_j) = (2 - \gamma - n_j)^{2-F}$ when $(-\gamma < n - a < 1 - \gamma)$ and vanishes otherwise; $w_0(n_j, n_l) = 1$ when $(n_l < 2 - 2\gamma - n_j)$ and vanishes otherwise. In our simulations, we use the optimal ZPE parameter $\gamma = 1/3$ for the triangle window function [14]. Note that the normalization condition of the total population is not satisfied for a single SQC trajectory, which may cause a difference between dynamics governed by the primitive and symmetrical MMST Hamiltonians.

2. Physical model systems

The spin-boson model is a commonly used two-level harmonic model for simulation of charge and energy transfer processes in complex molecular and condensed-phase systems [53,54]:

$$\hat{H} = \Gamma\hat{\sigma}_x + \varepsilon\hat{\sigma}_z + \sum_{i=1}^{N}\left(\frac{\hat{P}_i^2}{2} + \frac{1}{2}\omega_i^2\,\hat{R}_i^2 - c_i\hat{R}_i\hat{\sigma}_z\right), \tag{20}$$

where $\hat{\sigma}_x = |1\rangle\langle 2| + |2\rangle\langle 1|$ and $\hat{\sigma}_z = |1\rangle\langle 1| - |2\rangle\langle 2|$ are the Pauli matrices that are defined in the basis of the $|1\rangle$ and $|2\rangle$ basis; Γ is the electronic coupling coefficient; $\Delta E = -2\varepsilon$ is the reaction free energy; $\{\hat{R}_i, \hat{P}_i, \omega_i\} = \{\hat{R}_i, \hat{P}_i, \omega_i | i = 1, ..., N\}$ are the mass-weighted coordinates, momenta, and frequencies associated with the N nuclear normal modes, respectively; $\{c_i\}$ are the electronic-vibrational coupling coefficients. Here, $\{\omega_i, c_i\}$ are specified by discretizing the spectral density defined as

$$J(\omega) = \frac{\pi}{2}\sum_{i=1}^{N}\frac{c_i^2}{\omega_i}\delta(\omega - \omega_i). \tag{21}$$

In this work, we employ the Ohmic spectral density as below

$$J(\omega) = \frac{\pi}{2}\hbar\xi\omega e^{-\omega/\omega_c}, \tag{22}$$

where ξ is the Kondo parameter and ω_c is the cutoff frequency. The discretization scheme is as follows [55]

$$\omega_i = \omega_c \ln\left(\frac{N}{N-i+\frac{1}{2}}\right), \tag{23a}$$

$$c_i = \sqrt{\frac{\xi\hbar\omega_c}{N}}\omega_i, \tag{23b}$$

and i = 1, 2, · · · , N. The parameters for the spin-boson model tested are in reduced units: N = 100, ε = 1, Γ = 1, ξ = 0.1, ω_c = 2.5, $\hbar$ = 1, and the time step is Δt = 0.01.

In the semiclassical mapping dynamics simulation, the initial electronic state is $|1\rangle\langle 1|$, and the initial nuclear state is sampled from theWigner transform of the equilibrated bath density at inverse temperature $\beta = 1/k_BT = 5$:

$$\begin{aligned}\rho_N^{(W)}(\mathbf{R},\mathbf{P}) &= \int \mathrm{d}\mathbf{Z}\, e^{-i\mathbf{Z}\cdot\mathbf{P}/\hbar}\left\langle \mathbf{R}+\frac{\mathbf{Z}}{2}\middle|\hat{\rho}_N(0)\middle|\mathbf{R}-\frac{\mathbf{Z}}{2}\right\rangle \\ &= \prod_j^N \frac{1}{\pi\hbar}\tanh\left(\frac{\beta\hbar\omega_j}{2}\right) \\ &\quad \times \exp\left[-\frac{2}{\hbar\omega}\tanh\left(\frac{\beta\hbar\omega_j}{2}\right)\left(\frac{P_i}{2}+\frac{1}{2}\omega_i^2R_i^2\right)\right]. \end{aligned} \tag{24}$$

For the ML training, the nonadiabatic semiclassical simulations yield a training set of 500 independent CMM trajectories of length 1000 time steps starting from time zero for DD (GRU) and PINN (GRU and FCN) models, and a training set of 100 SQC trajectories for PINN (FCN) and 1800 SQC trajectories for DD (FCN) models. The test sets are another 1000 trajectories from both CMM and SQC dynamics. Training details can be found in Table I. The distribution of initial sampling of the electronic and nuclear variables for CMM and SQC dynamics in the training sets is shown in Fig. 2. The panels (a–c) and (d–f) show the initial samplings in CMM and SQC dynamics, respectively. In particular, panel (a) shows the sampled values of $(q_i^2 + p_i^2)$ /2 for the two states in CMM, which is related to electronic population distributions, and their sum is 1+$F\gamma$ depicted as a dashed line. Panel (b) indicates the distribution of the electronic mapping variables q_i, p_i for i = 1, 2 in CMM, which clearly shows the sampling over the constraint sphere. Panels (d) and (e) show the distribution of the action and angle mapping variables in SQC methods, where the action variables are drawn from the triangle window and the angle variables are randomly selected within $(-\pi/2, \pi/2]$. Panels (c) and (f) show the 30th nuclear phase-space variables distribution.

Table 1. ML training details including number of trajectories in training set Nts, hidden sizes Nh (same for NNs in DDNN and PINN), train and validation losses (MSE).

method	architecture	N_{ts}	N_h	train loss	valid loss
CMM	DD-FCN	500	(1024, 1024)	3.7×10^{-5}	3.5×10^{-5}
CMM	DD-GRU	500	(1024, 1024)	1.1×10^{-5}	1.2×10^{-5}
CMM	PINN-FCN	500	(1024, 1024)	1.0×10^{-6}	1.1×10^{-6}
CMM	PINN-GRU	500	(1024, 1024)	2.4×10^{-6}	2.4×10^{-6}
prim. SQC	PINN-FCN	100	(1024, 1024)	9.2×10^{-8}	8.7×10^{-8}
sym. SQC	DD-FCN	1800	(1024, 1024)	4.0×10^{-5}	4.0×10^{-5}
sym. SQC	PINN-FCN	100	(1024, 1024)	8.6×10^{-8}	1.0×10^{-7}

3. Results and discussion

We begin by presenting a comparative analysis of DD versus PINN approaches for learning the Markovian propagation in CMM dynamics of the spin-boson model. This comparison is crucial for understanding the efficacy of incorporating physical laws into machine learning frameworks for complex dynamical systems. Figure 3 illustrates the ensemble-averaged RDM dynamics, a key observable for characterizing the system's evolution. Both PINN models, one utilizing an FCN architecture and the other a GRU one, demonstrate excellent agreement with the reference CMM dynamics for the initial 6 Γ^{-1} of propagation. This timeframe includes several characteristic periods of the system's dynamics, indicating that the PINNs capture the essential short-to-intermediate time behavior accurately. Beyond this 6 Γ^{-1} point, while minor deviations from the reference CMM dynamics begin to appear, the discrepancies between the PINN-FCN and PINN-GRU predictions remain notably smaller than their respective deviations from the true CMM dynamics. This observation indicates the consistent and robust performance achieved by the two distinct PINN architectures, suggesting that the benefit stems from the physics-informed approach itself rather than a specific neural network design.

In contrast, both purely DD approaches struggle significantly to accurately capture the dynamics, even at the ensemble-averaged level. The DD-FCN model, while showing a semblance of accuracy by tracking the reference dynamics through the first two oscillatory periods (up to approximately 4 Γ^{-1}), subsequently undergoes a rapid and pronounced deterioration. It completely fails to predict the phase and amplitude of subsequent oscillations, rendering its long-term predictions unreliable. The DD-GRU network exhibits even poorer performance. It shows significant deviations from the reference dynamics almost immediately, failing to accurately capture even the first peak around 1.5 Γ^{-1}. Furthermore, it aberrantly settles into an unphysical, non-evolving steady state from approximately 4 Γ^{-1} onwards, a behavior entirely inconsistent with the expected dynamics of the spin-boson model. These results clearly demonstrate the superior capability of the PINN framework. By embedding the EOMs, PINNs accurately capture the stepwise time evolution of CMM mapping dynamics even with a relatively small training dataset of only 500 trajectories. This highlights a significant advantage in terms of data efficiency when compared to purely DD methods, which typically require substantially more data to achieve comparable accuracy, if at all.

The inherent advantages of the PINN methodology become even more pronounced and critically apparent when examining single trajectory predictions, as depicted in detail in Fig. 4. Analyzing individual trajectories provides a more stringent test of the models because propagation errors are not obscured or averaged out by ensemble statistics. Furthermore, there is no opportunity for fortuitous error cancellation that can sometimes occur when averaging over multiple, potentially inaccurate, trajectories. Both PINN-FCN and PINN-GRU variants accurately reproduce the intricate details of the reference mapping dynamics for a selection of nuclear positions (R_{10},R_{30},R_{60},R_{90}) and their corresponding canonical momenta (P_{10},P_{30},P_{60},P_{90}). These selected modes represent a range of frequencies within the nuclear bath modes, demonstrating the PINNs' ability to handle diverse dynamical behaviors. Some minor discrepancies, such as overly damped oscillations observed in the high-frequency modes, particularly at longer simulation times, are present. These are likely attributable

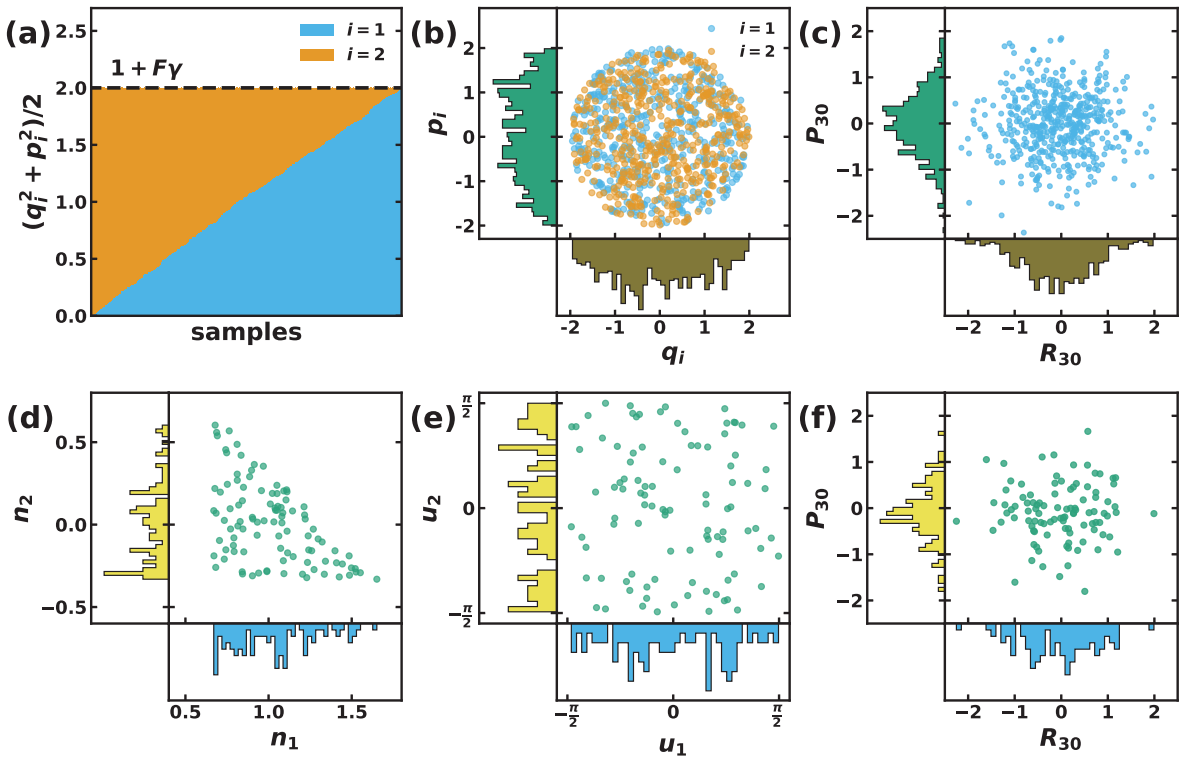

Figure 2. Distribution of the initial sampling for the CMM (a–c) and SQC (d–f) mapping dynamics in the training set. For CMM dynamics: (a) Distribution of $(q_i^2+p_i^2)/2$ for i = 1, 2 states and their sum $\Sigma_i^F(q_i^2+p_i^2)/2 = 1 + F\gamma$ as required for the electronic population restriction in CMM, where the x-axis is sorted index of samples; (b) Distribution of q_i and p_i for i = 1, 2, the histograms on the side are plotted for i = 0,1 together; (c) Phase space distribution of initial nuclear sampling of the 30th normal mode. For SQC dynamics: (d) Distribution of the action variables n_1,n_2 that fall in the triangle window by definition; (e) Distribution of the angle variables u_1,u_2 that are sampled randomly between $(-\pi/2, \pi/2]$; (f) Phase space distribution of initial nuclear sampling of the 30th normal mode.

to the inevitable accumulation of small numerical propagation errors over extended periods, a common challenge in long-term trajectory simulations, though significantly mitigated by the PINN approach. Importantly, the electronic mapping variables (q_1,p_1,q_2, p_2) for the two level electronic system are also well-predicted by both PINN chemes. The accurate propagation of these electronic degrees of freedom is absolutely essential for correctly reproducing the population dynamics and other electronic properties of the nonadiabatic system. Moreover, a key success of the PINN approach is that the inherent physical connections and correlations between position variables and their conjugate momenta are well-preserved throughout the simulation. This fidelity in maintaining the correct phase-space structure is a direct consequence of the PINN architecture being guided by the Hamiltonian structure embedded within the EOMs, which inherently dictates these fundamental relationships.

Conversely, the DD approaches, whether employing FCN or GRU architectures, completely fail to provide physically meaningful or even qualitatively correct predictions for single CMM trajectories, as vividly illustrated by the erratic paths in Fig. 4. The predictions often diverge rapidly from the reference or exhibit entirely unphysical behaviors. For instance, a striking example of this failure is seen in the DD-GRU model's prediction for the nuclear coordinate R_{10}. It incorrectly predicts R_{10} to move in the negative direction, despite its conjugate momentum P_{10} being positive at the initial time, which is a clear and fundamental violation of basic classical mechanics. Similar unphysical behaviors, such as incorrect directional propagation or loss of correlation between coordinates and momenta, are observed for other nuclear phase space variable pairs (e.g., R_{30} and P_{30}). These failures reflect the inability of the DD models, with limited data, to learn the underlying physical laws governing the system's evolution. While it is conceivable that the performance of DD approaches might be enhanced with access to a significantly larger training dataset, the primary focus of this comparative study is to evaluate the performance of DD and PINN methodologies under conditions of limited data availability. It is precisely in such low-data regimes that the benefits of incorporating prior physical knowledge, as done in PINNs, become most apparent and impactful.

Finally, we investigated whether the choice between two distinct formulations of the EOM for the MMST mapping Hamiltonian influences the performance and applicability within the PINN framework. These two formulations correspond to the primitive (as detailed in Eq. 2) and the symmetrized (as detailed in Eq. 4) MMST Hamiltonians. The primitive version explicitly includes the ZPE parameter, γ, directly in the EOM, which is then learned as a parameter by the neural network. In contrast, the symmetrized version does not explicitly feature γ in its EOM; instead, it requires the average potential energy function, $\bar{V}(\mathbf{R})$, which is then represented and learned by a neural network. Figure 5 presents a direct comparison of these two EOM types when applied to SQC mapping dynamics of the spin-boson model. The results compellingly indicate that the PINN-FCN approach performs effectively and yields accurate dynamics with both types of MMST Hamiltonians. The predicted population dynamics are in good agreement with their respective reference SQC calculations, regardless of whether the primitive or symmetrized Hamiltonian was used to inform the PINN. This outcome is significant as

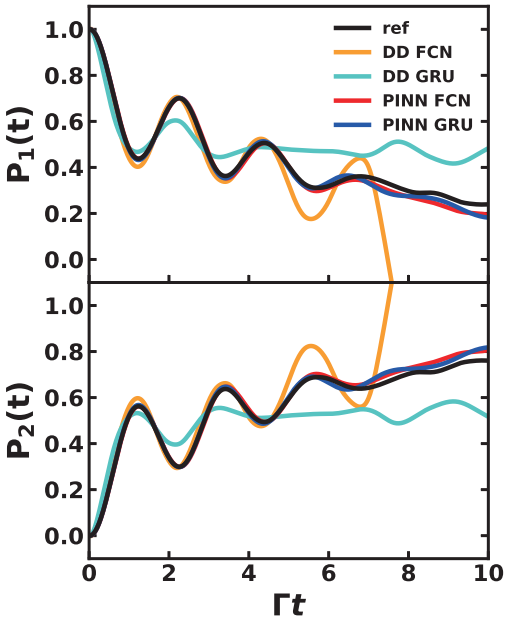

Figure 3. Ensemble-averaged RDM dynamics (over 1000 trajectories) of spin-boson model using different ML approaches. The reference CMM dynamics is plotted in a black line, and the predicted dynamics of DD-GRU, PINN-FCN, and PINN-GRU are plotted in turquoise, red, and blue lines, respectively.

it numerically verifies the equivalence of the two Hamiltonian formulations when integrated into the ML-enhanced simulation context, showcasing the flexibility of the PINN approach. In contrast, the purely Data-Driven FCN network exhibits a substantial deviation from the reference SQC population dynamics, with errors becoming apparent as early as 2 Γ^{-1}. Furthermore, the DD-FCN predictions show a more favorable trend in the long-term dynamics of SQC compared to the DD results for CMM dynamics, despite noticeable noise. This apparent improvement is likely due to the triangle window filtering scheme, which filters out unphysical predictions when the action mapping variable **n** falls outside the defined window. The scheme averages over a smaller number of mapping trajectories relative to the total available, which contributes to the observed noise in the longterm SQC dynamics. These state-dependent constraints on the mapping variables are essential for accurate observable calculations in SQC. However, the DD model does not explicitly incorporate such constraints, which reduces sampling effectiveness and leads to increased noise. Instead, the DD model must attempt to infer these complex conditions purely from the provided trajectory data, a significantly more demanding task, especially with limited training examples. The lack of explicit enforcement of such physical constraints contributes to the observed deviations and noise, further highlighting the advantages of the physics-informed strategy.

4. Concluding remarks

In conclusion, this work has demonstrated the significant advantages of employing PINN over purely DD approaches for learning the Markovian propagation of nonadiabatic semiclassical mapping dynamics, particularly when constrained by limited training data. Our findings reveal that PINNs, by incorporating the underlying equations of motion, consistently achieve high fidelity in predicting both ensemble-averaged RDM dynamics and the fine-grained details of single trajectories for the spin-boson model using the CMM framework. This accuracy extends across different neural network architectures (FCN and GRU) and is robust to the choice between primitive and symmetrized MMST Hamiltonian formulations within the SQC mapping context. In contrast, DD methods largely failed to produce physically meaningful or accurate predictions under identical training conditions, highlighting their inefficiency and unreliability in low-data regimes for such complex physical systems. These results emphasize the critical role of embedding physical laws into machine learning models to ensure accuracy, data efficiency, and physical consistency in simulating complex

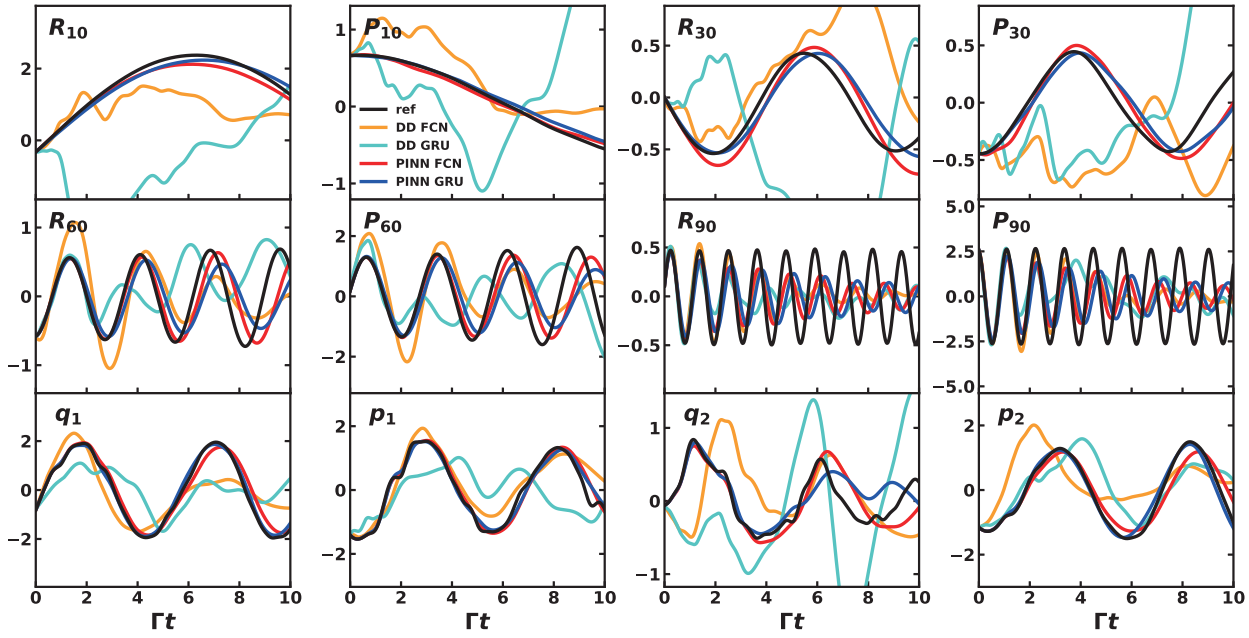

Figure 4. Single trajectory mapping dynamics of spin-boson model using different ML approaches. The reference CMM dynamics is plotted in a black line, and the predicted dynamics of DD-GRU, PINN-FCN, and PINN-GRU are plotted in turquoise, red, and blue lines, respectively. Four nuclear modes are selected to represent NN's performances for low, medium, and high frequency modes.

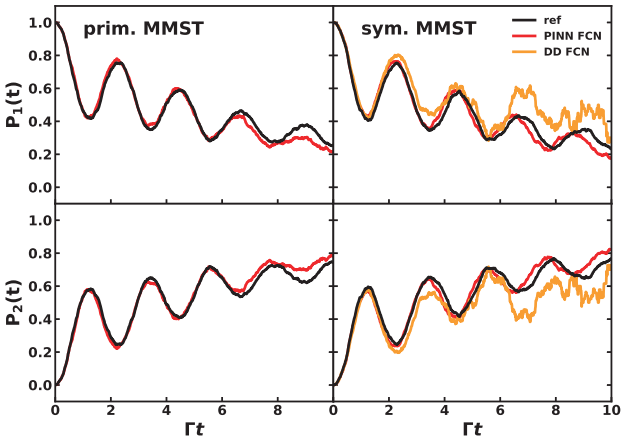

Figure 5. Ensemble-averaged RDM dynamics (over 1000 trajectories) of spin-boson model using different ML approaches. The reference SQC dynamics with primitive (left) and symmetrical (right) MMST EOM are plotted in black lines, and the predicted dynamics of DDFCN and PINN-FCN are plotted in orange and red lines, respectively.

molecular processes, paving the way for more reliable and powerful computational tools in nonadiabatic dynamics.

Acknowledgments

X.S. acknowledges support from the National Natural Science Foundation of China (No. 22273059). Computing resources were provided by NYU Shanghai HPC.

References

[1] Liu X.-Y., Chen W.-K., Fang W.-H., Cui G., Nonadiabatic dynamics simulations for photoinduced processes in molecules and semiconductors: methodologies and applications. *J. Chem. Theory Comput*., **19** (2023), 8491-8522.

[2] Mahadevan S., Liu T., Pratik S.M., Li Y., Ho H.Y., Ouyang S., Lu X., Yip H.-L., Chow P.C.Y., Brédas J.-L., Coropceanu V., So S.K., Tsang S.-W., Assessing intra and inter molecular charge transfer excitations in non fullerene acceptors using electroabsorption spectroscopy. *Nat. Commun*., **15** (2024), 2393.

[3] Zhang C., Zhong Y., Tao Z.-G., Qin X., Shang H., Lan Z., Prezhdo O.V., Gong X.-G., Chu W., Xiang H., Advancing nonadiabatic molecular dynamics simulations in solids with E(3) equivariant deep neural Hamiltonians. *Nat. Commun*., **16** (2025), 2033.

[4] Li J., Ji Q., Wang R., Zhang Z.-G., Wang X., Xiao M., Lu Y.-Q., Zhang C., Charge generation dynamics in organic photovoltaic blends under one sun equivalent illumination detected by highly sensitive terahertz spectroscopy. *J. Am. Chem. Soc*., **146** (2024), 20312-20322.

[5] Zhu R., Li W., Zhen Z., Zou J., Liao G., Wang J., Wang Z., Chen H., Qin S., Weng Y., Quantum phase synchronization via exciton vibrational energy dissipation sustains long lived coherence in photosynthetic antennas. *Nat. Commun*., **15** (2024), 3171.

[6] Meyer H.-D., Miller W.H., A classical analog for electronic degrees of freedom in nonadiabatic collision processes. *J. Chem. Phys*., **70** (1979), 3214-3223.

[7] Stock G., Thoss M., Semiclassical description of nonadiabatic quantum dynamics. *Phys. Rev. Lett*., **78** (1997), 578-581.

[8] Sun X., Wang H., Miller W.H., Semiclassical theory of electronically nonadiabatic dynamics: results of a linearized approximation to the initial value representation. *J. Chem. Phys*., **109** (1998), 7064-7074.

[9] Shi Q., Geva E., Nonadiative electronic relaxation rate constants from approximations based on linearizing the path integral forward backward action. *J. Phys. Chem. A*, **108** (2004), 6109-6116.

[10] Saller M.A.C., Kelly A., Richardson J.O., On the identity of the identity operator in nonadiabatic linearized semiclassical dynamics. *J. Chem. Phys*., **150** (2019), 071101.

[11] Gao X., Saller M.A.C., Liu Y., Kelly A., Richardson J.O., Geva E., Benchmarking quasiclassical mapping Hamiltonian methods for simulating electronically nonadiabatic molecular dynamics. *J. Chem. Theory Comput*., **16** (2020), 2883-2895.

[12] Hu Z., Sun X., All atom nonadiabatic semiclassical mapping dynamics for photoinduced charge transfer of organic photovoltaic molecules in explicit solvents. *J. Chem. Theory Comput*., **18** (2022), 5819-5836.

[13] Cotton S.J., Miller W.H., Symmetrical windowing for quantum states in quasi classical trajectory simulations: application to electronically non adiabatic processes. *J. Chem. Phys.*, **139** (2013), 234112.

[14] Cotton S.J., Miller W.H., A new symmetrical quasi classical model for electronically non adiabatic processes: application to the case of weak non adiabatic coupling. *J. Chem. Phys.*, **145** (2016), 144108.

[15] Cotton S.J., Liang R., Miller W.H., On the adiabatic representation of Meyer Miller electronic nuclear dynamics. *J. Chem. Phys*., **147** (2017), 064112.

[16] Cotton S.J., Miller W.H., Trajectory adjusted electronic zero point energy in classical Meyer Miller vibronic dynamics: symmetrical quasi classical application to photodissociation. *J. Chem. Phys*., **150** (2019), 194110.

[17] Huang H., Peng J., Lan Z., Hu D., Liu Y.-J., Nonadiabatic dynamics of intersystem crossings with the symmetrical quasi classical dynamics method based on the Meyer Miller mapping Hamiltonian. *J. Chem. Theory Comput*., **21** (2025), 4386-4396.

[18] Liu J., A unified theoretical framework for mapping models for the multi state Hamiltonian. *J. Chem. Phys*., **145** (2016), 204105.

[19] He X., Liu J., A new perspective for nonadiabatic dynamics with phase space mapping models. *J. Chem. Phys*., **151** (2019), 024105.

[20] He X., Gong Z., Wu B., Liu J., Negative zero point energy parameter in the Meyer Miller mapping model for nonadiabatic dynamics. *J. Phys. Chem. Lett*., **12** (2021), 2496-2501.

[21] Liu J., He X., Wu B., Unified formulation of phase space mapping approaches for nonadiabatic quantum dynamics. *Acc. Chem. Res*., **54** (2021), 4215-4228.

[22] He X., Wu B., Shang Y., Li B., Cheng X., Liu J., New phase space formulations and quantum dynamics approaches. *WIREs Comput. Mol. Sci*., 12 (2022), e1619.

[23] Liu Z., Lyu N., Hu Z., Zeng H., Batista V.S., Sun X., Benchmarking various nonadiabatic semiclassical mapping dynamics methods with tensor train thermo field dynamics. *J. Chem. Phys*., **161** (2024), 024102.

[24] Kovacs D.P., Moore J.H., Browning N.J., Batatia I., Horton J.T., Pu Y., Kapil V., Witt W.C., Magdau I.-B., Cole D.J., Csányi G., MACE OFF: short range transferable machine learning force fields for organic molecules. *J. Am. Chem. Soc*., **147** (2025), 17598-17611.

[25] Zeng J., Zhang D., Peng A., Zhang X., He S., Wang Y., Liu X., Bi H., Li Y., Cai C., et al., DeePMD kit v3: a multiple backend framework for machine learning potentials. *J. Chem. Theory Comput*., **21** (2025), 4375-4385.

[26] Zou Z., Zhang Y., Liang L., Wei M., Leng J., Jiang J., Luo Y., Hu W., A deep learning model for predicting selected organic molecular spectra. *Nat. Comput. Sci*., **3** (2023), 957-964.

[27] Westermayr J., Marquetand P., Machine learning for electronically excited states of molecules. *Chem. Rev*., **121** (2021), 9873-9926.

[28] Li J., Lopez S.A., A look inside the black box of machine learning photodynamics simulations. *Acc. Chem. Res*., **55** (2022), 1972-1984.

[29] Li S., Xie B.-B., Yin B.-W., Liu L., Shen L., Fang W.-H., Construction of highly accurate machine learning potential energy surfaces for excited state dynamics simulations based on low level data sets. *J. Phys. Chem. A*, **128** (2024), 5516-5524.

[30] Yao Q., Ji Q., Li X., Zhang Y., Chen X., Ju M.-G., Liu J., Wang J., Machine learning accelerates precise excited state potential energy surface calculations on a quantum computer. *J. Phys. Chem. Lett*., **15** (2024), 7061-7068.

[31] Zeng H., Kou Y., Sun X., How sophisticated are neural networks needed to predict long term nonadiabatic dynamics? *J. Chem. Theory Comput*., **20** (2024), 9832-9848.

[32] Wu D., Hu Z., Li J., Sun X., Forecasting nonadiabatic dynamics using hybrid convolutional neural network/long short term memory network. *J. Chem. Phys*., **155** (2021), 244104.

[33] Lin K., Peng J., Xu C., Gu F.L., Lan Z., Automatic evolution of machine learning based quantum dynamics with uncertainty analysis. *J. Chem. Theory Comput*., **18** (2022), 5837-5855.

[34] Tang D., Jia L., Shen L., Fang W.-H., Fewest switches surface hopping with long short term memory networks. *J. Phys. Chem. Lett*., **13** (2022), 10377-10387.

[35] Lin K., Peng J., Xu C., Gu F.L., Lan Z., Trajectory propagation of symmetrical quasi classical dynamics with Meyer Miller mapping Hamiltonian using machine learning. *J. Phys. Chem. Lett*., **13** (2022), 11678-11688.

[36] Herrera Rodríguez L.E., Kananenka A.A., Convolutional neural networks for long time dissipative quantum dynamics. *J. Phys. Chem. Let*t., **12** (2021), 2476–2483.

[37] Ullah A., Dral P.O., Speeding up quantum dissipative dynamics of open systems with kernel methods. *New J. Phys*., **23** (2021), 113019.

[38] Herrera Rodríguez L.E., Ullah A., Espinosa K.J.R., Dral P.O., Kananenka A.A., A comparative study of different machine learning methods for dissipative quantum dynamics. *Mach. Learn.: Sci. Technol*., **3** (2022), 045016.

[39] Cho K., Van Merrienboer B., Gulcehre C., Bahdanau D., Bougares F., Schwenk H., Bengio Y., Learning phrase representations using RNN encoder–decoder for statistical machine translation. *Proceedings of the 2014 Conference on Empirical Methods in Natural Language Processing (EMNLP)*, Association for Computational Linguistics, Doha, (2014), 1724-1734.

[40] Hochreiter S., Schmidhuber J., Long short term memory. *Neural Comput*., **9** (1997), 1735–1780.

[41] Lin K., Peng J., Gu F.L., Lan Z., Simulation of open quantum dynamics with bootstrap based long short term memory recurrent neural network. *J. Phys. Chem. Lett*., **12** (2021), 10225-10234.

[42] Herrera Rodríguez L.E., Kananenka A.A., A short trajectory is all you need: a transformer based model for long time dissipative quantum dynamics. *J. Chem. Phys*., **161** (2024), 171101.

[43] Raissi M., Perdikaris P., Karniadakis G.E., Physics informed deep learning (part I): data driven solutions of nonlinear partial differential equations. arXiv, 1711.10561 (2017).

[44] Raissi M., Perdikaris P., Karniadakis G.E., Physics informed neural networks: a deep learning framework for solving forward and inverse problems involving nonlinear partial differential equations. *J. Comput. Phys*., **378** (2019), 686-707.

[45] Karniadakis G.E., Kevrekidis I.G., Lu L., Perdikaris P., Wang S., Yang L., Physics informed machine learning. *Nat. Rev. Phys*., **3** (2021), 422-440.

[46] Cuomo S., Di Cola V.S., Giampaolo F., Rozza G., Raissi M., Piccialli F., Scientific machine learning through physics informed neural networks: where we are and what's next. *J. Sci. Comput*., **92** (2022), 88.

[47] Wang F., Zhai Z., Zhao Z., Di Y., Chen X., Physics informed neural network for lithium ion battery degradation stable modeling and prognosis. *Nat. Commun*., **15** (2024), 4332.

[48] Ullah A., Huang Y., Yang M., Dral P.O., Physics informed neural networks and beyond: enforcing physical constraints in quantum dissipative dynamics. *Digit. Discov*., **3** (2024), 2052-2060.

[49] Mulvihill E., Schubert A., Sun X., Dunietz B.D., Geva E., A modified approach for simulating electronically nonadiabatic dynamics via the generalized quantum master equation. *J. Chem. Phys*., **150** (2019), 034101.

[50] Brian D., Sun X., Generalized quantum master equation: a tutorial review and recent advances. *Chin. J. Chem. Phys*., **34** (2020), 497-524.

[51] Hu Z., Brian D., Sun X., Multi state harmonic models with globally shared bath for nonadiabatic dynamics in the condensed phase. *J. Chem. Phys*., **155** (2021), 124105.

[52] Liu Z., Sun X., Direct all atom nonadiabatic semiclassical simulations for electronic absorption spectroscopy of organic photovoltaic non fullerene acceptor in solution. *J. Phys. Chem. Lett*., **16** (2025), 4463-4473.

[53] Weiss U., *Quantum Dissipative Systems*, World Scientific, Singapore, 2012.

[54] Nitzan A., *Chemical Dynamics in Condensed Phases: Relaxation, Transfer and Reactions in Condensed Molecular Systems*, Oxford University Press, New York, 2006.

[55] Walters P.L., Allen T.C., Makri N., Direct determination of discrete harmonic bath parameters from molecular dynamics simulations. *J. Comput. Chem*., **38** (2017), 110-115.